RSC Advances

ROYAL SOCIETY OF CHEMISTRY

www.rsc.org/advances

Journal Name

RSCPublishing

ARTICLE

Biomimetic synthesis of C_3N_4/TiO_2/Ag nanosheet composites with high visible-light photocatalytic performance

Cite this: DOI: 10.1039/x0xx00000x

Received 00th January 2012,
Accepted 00th January 2012

DOI: 10.1039/x0xx00000x

www.rsc.org/

Zhen Wei Tong,[ad] Dong Yang,[bc] Yuan Yuan Sun,[bd] and Zhong Yi Jiang*[ad]

In order to more efficiently utilize the solar energy, the semiconductor−based nanocomposites with high visible−light response have attracted much interest in recent years. In this study, the C_3N_4/TiO_2/Ag nanosheet with high visible−light photocatalytic performance has been synthesized *via* a biomimetic strategy under mild conditions. Firstly, TiO_2 nanoparticles (NPs) about 10 nm in diameter are loaded on the C_3N_4 nanosheet by the arginine−enabled biomimetic mineralization. Then, Ag NPs about 5 nm in size nucleate and grow on the TiO_2 surface using 3−(3, 4−dihydroxyphenyl) propionic acid as an anchor and a reducer to form the TiO_2−Ag heterojunction. The resultant C_3N_4/TiO_2/Ag nanosheet exhibits significantly higher photoelectric conversion efficiency and photodegradation activity than pure C_3N_4 and C_3N_4/TiO_2 under visible−light irradiation. Moreover, the loading amount of Ag nanocrystals can be readily regulated by changing the $AgNO_3$ concentration. Both TiO_2 and Ag play critical roles for the enhanced photocatalytic activity of C_3N_4/TiO_2/Ag nanosheets. The band match of TiO_2 with C_3N_4 is in favour of the separation of photo−generated carriers in C_3N_4, and the surface plasmon resonance effect of Ag nanocrystals induces the electron excitation in TiO_2 NPs under visible light. This study offers a facile approach for the cost-effective and environmentally benign synthesis of high-efficiency photocatalysts.

Introduction

In the past few decades, the significant upsurge of visible−light photocatalysis has generated increasing attention due to its potential application in the environment and energy fields.[1-3] Since Antonietti and co−workers reported the optical property, electronic structure, and photocatalytic activity of C_3N_4 in 2009,[4] much effort has been focused on the application of C_3N_4 in the energy conversion, hydrogen and carbon dioxide storage and purification of contaminated water because of its visible−light driven bandgap (2.69 eV) and suitable conduction band position.[5-7] Moreover, C_3N_4, as a novel photocatalytic material, demonstrates higher thermal and chemical stability than various conventional visible−light photocatalysts, such as metal sulphide and N−doped TiO_2. However, C_3N_4 exhibits a high recombination rate of photo−generated electron/hole pairs and the limited quantum efficiency (3.5 % at 420-460 nm), which restrict its wide application in the photocatalysis.[8] In order to solve these problems, the C_3N_4−based composite material is becoming a burgeoning research area. Until now, many nanocomposites of C_3N_4 with other materials, such as oxides, [9,10] sulphides,[11,12] carbon materials,[2,13] and metals,[14] have been prepared for harvesting the high photocatalytic performance. For example, Liu *et al.* fabricated a C_3N_4/carbon nanodot composite, which demonstrated an overall solar energy conversion efficiency of 2.0% for photocatalytic solar water splitting.[2]

In the previous study, the C_3N_4/TiO_2 nanosheet was prepared by a facile biomimetic approach under relative mild conditions, and exhibited high degradation efficiency for RhB under simulated−sunlight irradiation.[15] However, their visible−light photocatalytic performance needs to be further improved, since TiO_2 nanoparticles in the composite cannot be excited by visible light. It is well−known that the heterojunction of wide−bandgap semiconductor with noble metals including Ag, Au, and Pt *et al.* can apparently enhance the visible−light absorbance (accounting for 43% of solar spectrum) by the surface plasmon resonance (SPR) photosensitization and inhibit the recombination of photo−generated carriers by the Schottky barrier formed between semiconductor and noble metal simultaneously.[1,16,17] Moreover, it was found that the noble metal can excite adjacent semiconductors *via* enhanced electric field amplitude.[16,18] Ag is one of the most promising noble metals for extensive application owing to its relative low cost, inherent antibacterial activity, and facile preparation. Therefore, it may be a good idea by using Ag nanocrystals to further improve the photocatalytic performance of C_3N_4/TiO_2 nanosheets. More recently, Chen *et al.*[19] constructed the g−C_3N_4/Ag/TiO_2 microsphere with enhanced visible−light photocatalytic performance, in which Ag NPs were photodeposited as the interlayer between g−C_3N_4 (as the outer layer with 4% mass ratio) and the surface of TiO_2 microspheres. However, this kind of microspherical structure is not beneficial to the light absorption and utilization, and the synthetic condition is not mild due to the

involvement of chemical solvents. It is desirable to develop a biomimetic strategy for the synthesis of $C_3N_4/TiO_2/Ag$ nanocomposites with the structure in favour of visible−light absorption and utilization.

In the present study, a $C_3N_4/TiO_2/Ag$ composite system based on a grafted nanosheet structure (commonly used in the graphene composite catalysts) has been first synthesized by a biomimetic strategy. The C_3N_4/TiO_2 nanosheet was first prepared by the arginine−enabled biomimetic mineralization, and then loaded Ag nanoparticles assisted by 3−(3, 4−dihydroxyphenyl) propionic acid (diHPP) to form the $C_3N_4/TiO_2/Ag$ nanosheet under mild conditions. DiHPP can link to the TiO_2 surface *via* the bi−dentate chelation of catechol group with Ti^{4+}, and act as both an anchor and a reducer to *in situ* nucleate and grow Ag nanocrystals on the TiO_2 surface under ambient conditions.[20,21] The morphology and structure of the $C_3N_4/TiO_2/Ag$ nanosheet were characterized, and the photoelectric and photocatalytic performance of $C_3N_4/TiO_2/Ag$ nanosheet were investigated. Moreover, a tentative photocatalytic mechanism was also proposed.

Experimental

Synthesis of $C_3N_4/TiO_2/Ag$

Graphite–like C_3N_4 powders were prepared according to the literature.[22] In specific, melamine (10.0 g) was put into an alumina crucible with a cover, and calcined at 550 °C for 4 h with a heating rate of 2.5 °C min^{-1} in air in a muffle furnace. The resulting yellow product g−C_3N_4 was collected and ground into powder for further synthesis. The C_3N_4/TiO_2 nanosheet was prepared by a biomimetic method reported in our previous work.[15] In brief, g–C_3N_4 (0.560 g) was added into deionized water (5 mL), and sonicated for 10 min. Then, arginine solution (pH=7.0) (20 mL, 0.3 mol L^{-1}) was mixed with the C_3N_4 suspension under magnetic stirring for 3 h at room temperature. After adding Ti−BALDH (1 mL, 0.25 mol L^{-1}) solution into the suspension and stirring for 30 min, the composite of g−C_3N_4 loaded with amorphous TiO_2 was fabricated, which is denoted as g−C_3N_4/am−TiO_2. The g−C_3N_4/am−TiO_2 precipitate was collected by centrifugation, washed with deionized water, and freeze−dried in a vacuum freeze drier for 8 h. After calcining g−C_3N_4/am−TiO_2 at 480 ºC for 2 h with a rate of 5 ºC min^{-1}, the C_3N_4/TiO_2 nanosheet was prepared finally.

Fifty milligram as-prepared C_3N_4/TiO_2 nanosheet was mixed with deionized water (10 mL) under magnetic stirring. Then, diHPP solution (2 mL, 2 mg mL^{-1}) was added in the suspension and vigorously stirred for 30 min, which is superfluous for saturatedly adsorbing on the surface of C_3N_4/TiO_2 nanosheet. The C_3N_4/TiO_2 nanosheet modified by diHPP was centrifuged, washed with deionized water to remove unadsorbed diHPP, and re-dispersed in deionized water (10 mL). Subsequently, $AgNO_3$ solution (10 mL) was added to the suspension and kept stirring for 24 h at room temperature, during which its color changed from yellow to gray. The product was then isolated by centrifugation, washed and freeze-dried for 8 h. At last, five samples were prepared in the $AgNO_3$ solution with different concentrations (0.5, 1.0, 2.0, 3.0, and 5.0 mmol L^{-1}), which are denoted as $C_3N_4/TiO_2/Ag$−X (X=0.5, 1, 2, 3, 5), respectively. The amount of loading Ag in the nanosheets is 0.91%, 2.06%, 3.81%, 5.37% and 8.76%, tested by ICP later. For comparison, the C_3N_4/Ag nanosheet (C_{Ag^+}=3 mmol L^{-1}) was also prepared under the same conditions except substituting C_3N_4 nanosheet for C_3N_4/TiO_2. In addition, a physically mixed sample (denoted as PMS) was also prepared by mixing about 70 wt % C_3N_4/Ag with 30 wt % TiO_2 nanoparticles (Fig. S1a).

Characterization

High resolution transmission electron microscopy (HRTEM) and energy dispersive X-ray analysis spectroscopy (EDS) were conducted at 90 K using a JEOL-2011 equipped with a Bruker X-flash silicon drift detector (SDD) at 200 kV. The crystal form of these samples was characterized by X-ray diffraction spectroscopy (XRD) with a Rigaku D/max 2500V/PC X-ray diffractometer (Cu Kα, λ = 0.154 nm, 40 kV, 200 mA). Fourier transform infrared spectroscopy (FTIR) was measured on a Nicolet-560 spectrometer. The chemical status and element composition of the sample were analyzed by X-ray photoelectron spectroscopy (XPS, Perkin-Elmer PHI 1600 ESCA with monochromatized Mg Kα radiation (1253.6 eV). The diffuse-reflectance spectrum (DRS) was recorded with a UV-vis spectrophotometer (U-3010, Hitachi) equipped with an integrating sphere, using $BaSO_4$ as the reference. Thermo-gravimetric analysis (TGA) was performed with a Perkin-Elmer TG/DTA thermo-gravimetric analyzer by heating from 20 to 800 °C at a rate of 10 °C min^{-1} in air atmosphere.

Photoelectrochemical measurements

To measure the photocurrent generation response and the electrochemical impedance spectra (EIS), the film electrodes of photocatalysts were firstly prepared. The doctor-blade technique was employed to prepare the film on the F-doped tin oxide (FTO) coated glass substrate (2 cm×2 cm). The slurry consisting of 30 mg sample, 1 drop of Triton X-100 and 1 drop of acetylacetone were deposited on the substrate twice. The active area of the film was ca. 1.0 cm^2. After coating, the films were sintered in air at 380 °C for 1 h. Photoelectrochemical measurements were carried out using an electrochemical workstation (CHI 660C Shanghai Chenhua) in a standard three-electrode cell system. The resultant electrode was employed as the working electrode. Meanwhile, a platinum wire electrode and a saturated Ag/AgCl electrode served as the counter and reference electrode, respectively. A 0.1 mol L^{-1} KCl aqueous solution was employed as the electrolyte. The working electrode was irradiated by a 300 W Xe lamp (PLS-SXE300). The EIS was operated at open circuit potential. The generated photocurrent was recorded by a computer-controlled potentiostat. The amplitude of the sinusoidal wave is 5.0 mV and the frequency range examined is from 100 kHz to 0.1 Hz.

Photocatalytic activity

Photocatalytic activities of as−prepared samples were evaluated by the degradation of RhB (10 mg L^{-1}) and MB (7.46 mg L^{-1}) in aqueous solution under 500 W Xe lamp (Beijing AuLight Technology Co.) with a cutoff filter (λ>420 nm), respectively. The light intensity was determined to be 0.15 mW cm^{-2} at 420 nm by using a UV-A radiometer (Photoelectric Instrument Factory, Beijing Normal University, model UV-A). Fifteen milligram photocatalysts were dispersed in 25 mL dye solution in a 50 mL quartz tube. Prior to irradiation, the

suspension was magnetically stirred for 30 min in the dark to ensure that the photocatalyst surface was saturated with organic dyes. Every irradiation interval, 2.0 mL suspension was sampled, and the dye concentration was analyzed with a UV-vis spectrophotometer (Hitachi, U-3010) at the maximal absorption wavelength of dye.

To investigate the role of photo-generated radical species in the photocatalytic degradation of dye, a series of controlled experiments were further performed. Three radical scavengers including methanol (1: 15/v: v), disodium ethylenediaminetetraacetate (EDTA, 10 mmol L^{-1}) and benzoquinone (1 mmol L^{-1}) were added into the reaction system to investigate the specific reactive specie ·OH, h^+ and $·O_2^-$ involved in the RhB degradation over $C_3N_4/TiO_2/Ag$ photocatalyst, respectively. Furthermore, the changes of UV-Vis absorption spectra of RhB over $C_3N_4/TiO_2/Ag$ photocatalyst were tested to confirm the RhB degradation pathway.

Results and Discussion

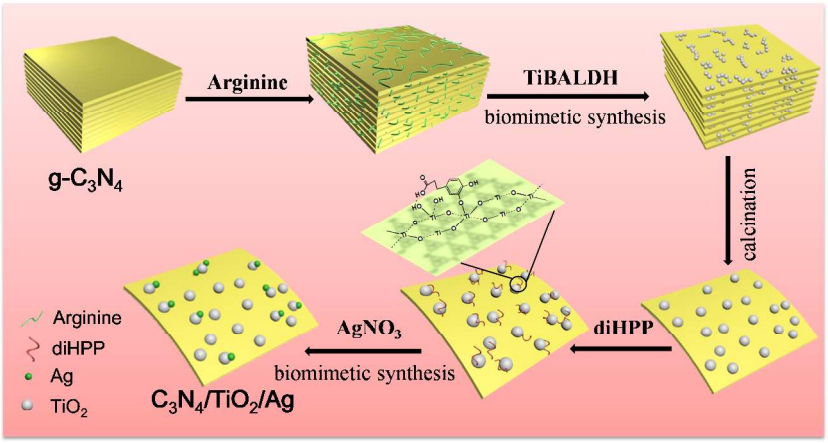

Scheme 1. The synthetic procedure for $C_3N_4/TiO_2/Ag$ nanosheet photocatalyst.

Scheme 1 illustrates the schematic diagram for the synthetic procedure of $C_3N_4/TiO_2/Ag$ nanosheet composites by a biomimetic strategy. At first, bulk graphite C_3N_4 (g-C_3N_4) is synthesized by calcining the melamine at high temperature. Then, arginine molecules are adsorbed on the bulk g−C_3N_4 surface and inserted in the g−C_3N_4 layers *via* the electrostatic interaction, which can induce the hydrolysis and polycondensation of titanium precursor (Ti−BALDH) to form TiO_2 nanoparticles at room temperature. The obtained g−C_3N_4/am−TiO_2 composite is treated at high temperature for the g−C_3N_4 delamination and TiO_2 crystallization simultaneously, thus resulting in the formation of C_3N_4/TiO_2 nanosheet. Afterwards, C_3N_4/TiO_2 is suspended in an aqueous solution of diHPP, a kind of environmentally−friendly organic molecule, and then its colour changes from white to orange gradually, apparently suggesting the successful adsorption of diHPP on the C_3N_4/TiO_2 surface. It is inferred that the diHPP is preferentially adsorbed on the surface of TiO_2 nanoparticles *via* the bi−dentate chelation of catechol group with Ti^{4+}.[16,23] Subsequently, the diHPP−functionalized C_3N_4/TiO_2 is dispersed in the $AgNO_3$ solution, in which the diHPP acts as both an anchor and a reducer to *in situ* nucleate and grow Ag nanocrystals on the C_3N_4/TiO_2 surface.[21] After stirring for 24 h, the suspension colour changes from orange to grey, indicating the generation of Ag nanocrystals. Finally, the $C_3N_4/TiO_2/Ag$ nanosheet composite is synthesized.

Morphology and structure

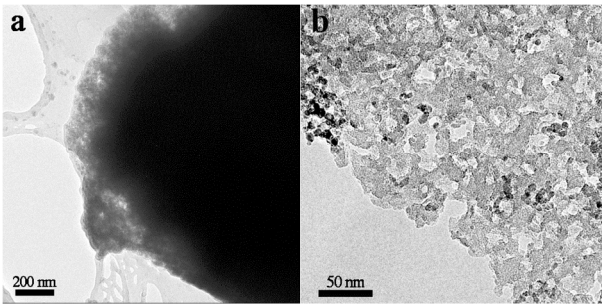

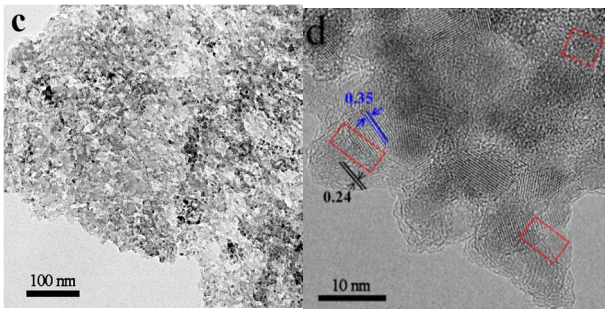

Fig. 1 TEM images of (a) g−C_3N_4/am−TiO_2, (b) C_3N_4/TiO_2 and (c) C_3N_4/TiO_2/Ag-3; (d) HRTEM image of C_3N_4/TiO_2/Ag-3 sample.

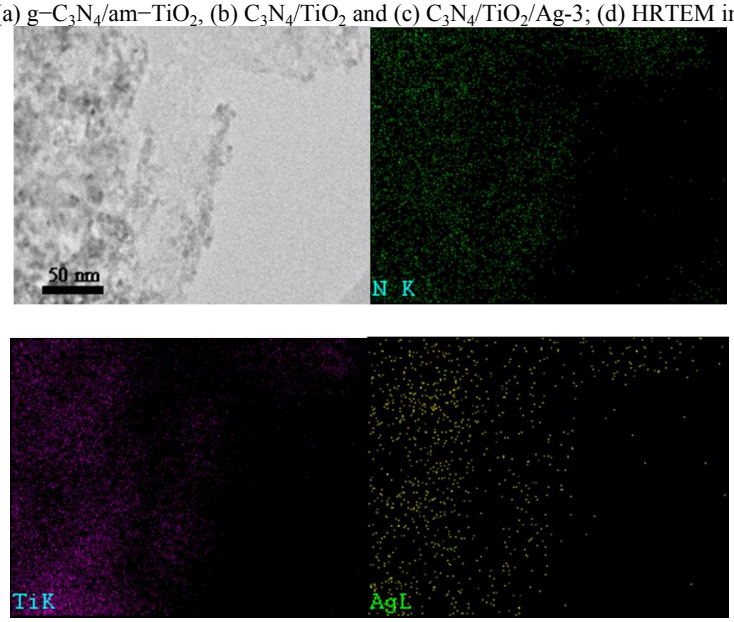

Fig. 2 STEM−EDX mapping of C_3N_4/TiO_2/Ag−3 nanosheet.

As illustrated in Fig. 1a, the g−C_3N_4/am−TiO_2 appears as a bulk material before thermal treatment; while the C_3N_4/TiO_2 exhibits a nanosheet structure, in which many nanoparticles uniformly distribute on the C_3N_4 nanosheet (Fig. 1b).[15] Moreover, the C_3N_4/TiO_2 nanosheet has some nanopores, likely arising from the decomposition of its unstable area during the thermal treatment.[24] The thickness of pure C_3N_4 nanosheet is determined to be about 1.762 nm (about five layers) *via* AFM analysis (Fig. S2), which should be close to that of C_3N_4/TiO_2. Figure 1c demonstrates a typical TEM image of C_3N_4/TiO_2/Ag−3, in which many nanoparticles disperse on the C_3N_4 nanosheet. From its HRTEM photo (Fig. 1d), two lattice fringes about 0.35 and 0.24 nm can be distinctly identified, in agreement with the spacing of (101) plane of anatase TiO_2 (JCPDS NO. 21−1272) and (111) plane of cubic Ag (JCPDS NO. 04−0783), respectively. These TiO_2 nanoparticles are about 10 nm in size, and intimately graft onto the C_3N_4 support; while most of Ag nanoparticles about 5 nm in size grow on the TiO_2 and C_3N_4 surfaces. It is worthy of noting that a heterojunction structure can be clearly observed between TiO_2 and Ag (red box in Fig. 1d). It is known that the diHPP molecules tend adsorb on the TiO_2 surface *via* the strong chelation effect between TiO_2 and diHPP, and then induced the formation of well−crystallized Ag nanoparticles.[21] Therefore, most of Ag nanoparticles form the heterojunction with TiO_2 in the C_3N_4/TiO_2/Ag nanosheet, and only a little part of Ag grow on C_3N_4 surface. In order to further analyze the distribution of each component in the C_3N_4/TiO_2/Ag, the STEM−EDS element mapping was conducted. From Fig. 2, it can be seen that the N and Ti elements are present at the bottom with a uniform lateral intensity, while the Ag element distributes on the outer surface with a lower intensity. This result further confirms that TiO_2 nanoparticles anchor on the C_3N_4 nanosheet, and Ag nanoparticles tend to gather around TiO_2.

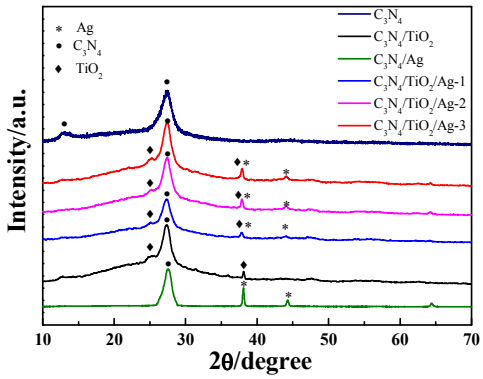

Fig. 3 XRD patterns of pure C_3N_4, C_3N_4/TiO_2, C_3N_4/Ag and C_3N_4/TiO_2/Ag samples.

In order to investigate the composition and crystallographic structure of as−prepared C_3N_4/TiO_2/Ag samples, the XRD was performed (Fig. 3). In the XRD curve of pure C_3N_4, the peak at 27.3° is attributed to the (002) plane of C_3N_4, which origins from the interlayer stacking of the conjugated aromatic system;[25] while the peak at 12.9° is indexed as the (100) plane of tri−s−triazine.[26] Two peaks at 24.9° and 38.1° are detectable in all of samples containing TiO_2,[27] which are the characteristic peaks of anatase TiO_2. Compared with that of C_3N_4/TiO_2, the XRD patterns of C_3N_4/TiO_2/Ag exhibit a new peak at 44.1°, which can be assigned to the (200) plane of cubic Ag crystal. Since the loading amount of TiO_2 and Ag nanoparticles on the C_3N_4 nanosheet is low, their diffraction peaks are weak.

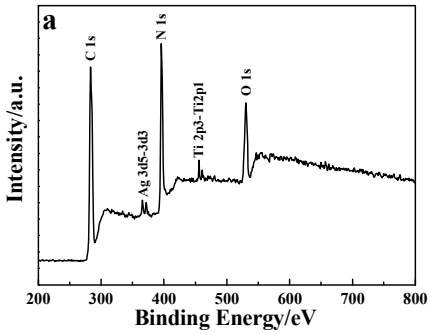

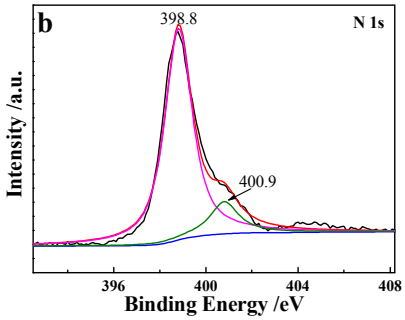

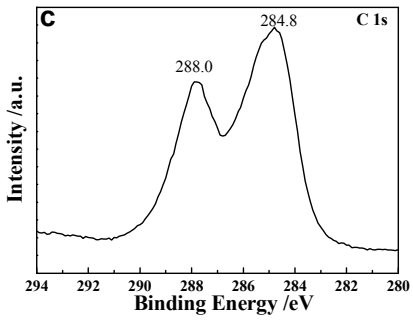

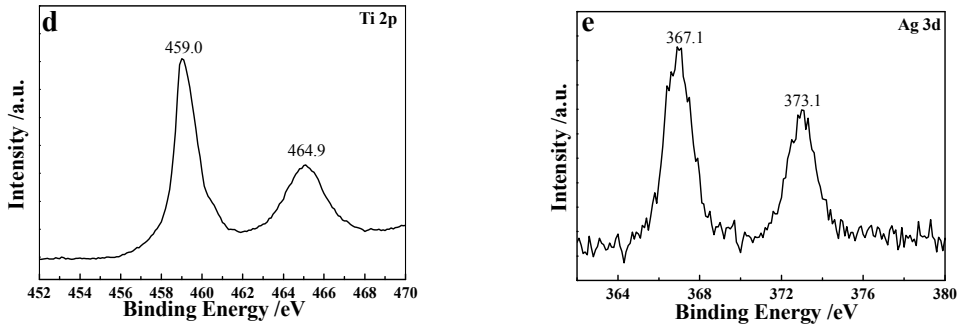

Fig. 4 XPS spectra of $C_3N_4/TiO_2/Ag$: (a) survey scan spectrum and high−resolution spectra of (b) N1s, (c) C 1s, (d) Ti 2p and (e) Ag 3d.

The XPS was carried out to further determine the element composition and analyze the chemical status of various elements in the as−prepared $C_3N_4/TiO_2/Ag$ samples. The C, N, O, Ti, and Ag elements can be found in the survey scan XPS spectrum of $C_3N_4/TiO_2/Ag$-3 (Fig. 4a), and the high−resolution XPS spectra of N 1s, C 1s, Ti 2p, and Ag 3d were shown in Fig. 4b−e. The high−resolution N 1s curve can be deconvolved into two peaks at 398.8 and 400.9 eV by using Gaussian−Lorentzian peak fitting (Fig. 4b). The former originates from the sp^2−hybridized N (C−N=C), while the latter can be attributed to the tertiary N (N−$(C)_3$).[19] Both of them consist of the heptazine heterocyclic ring C_6N_7, the basic substructure unit of C_3N_4. There are two main peaks at 284.8 and 288.0 eV in Fig. 4c, which can be ascribed to the sp^3−hybridized C−C bond and sp^2−hybridized C in the triazine ring (N–C=N), respectively.[24] The high−resolution Ti 2p curve (Fig. 4d) also demonstrates two peaks at 459.0 and 464.9 eV, which belong to the Ti 2p3/2 and Ti 2p1/2 orbits, respectively, indicating the presence of Ti^{4+}.[28] As demonstrated in Fig. 4e, the Ag 3d spectrum has two peaks at 367.1 and 373.1 eV, belonging to the Ag 3d5/2 and Ag 3d3/2 orbits, respectively. The splitting of Ag 3d doublet about 6 eV confirms that the Ag element is present as Ag^0 in the $C_3N_4/TiO_2/Ag$ sample.[29] It is noted that compared to those of bulk Ag^0 materials (368.3 eV for Ag 3d5/2 and 374.3 eV for Ag 3d3/2), these two peaks exhibit a negative shift. It is deduced that some electrons may transfer from TiO_2 to metallic Ag through the Ag−TiO_2 heterojunction, resulting in the binding energy shift of Ag 3d.

Photoabsorption and photoelectric performance

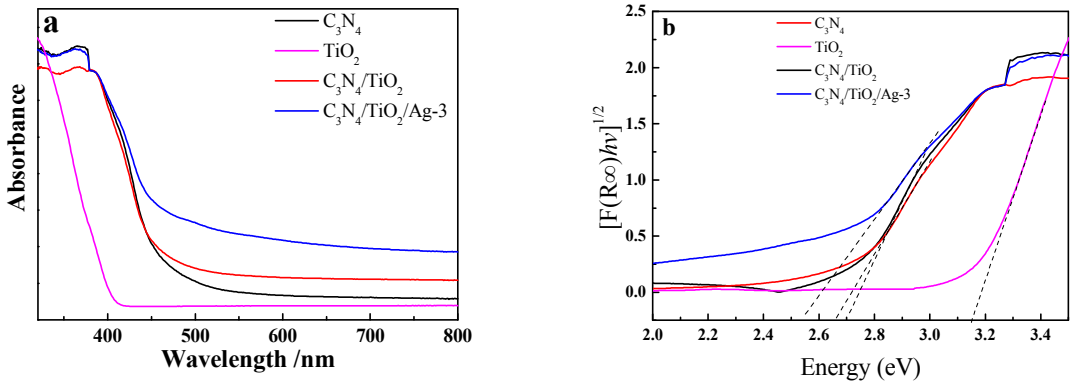

Fig. 5 (a) DRS of C_3N_4, TiO_2, C_3N_4/TiO_2 and $C_3N_4/TiO_2/Ag$-3 and (b) their corresponding plots of [F(R∞)hv]1/2 versus hv.

Figure 5a illustrates the DRS of pure C_3N_4, TiO_2, C_3N_4/TiO_2 and $C_3N_4/TiO_2/Ag$−3. It is clear that pure TiO_2 only absorbs UV light, while other three samples containing C_3N_4 can absorb the light from UV through visible range up to 460 nm. In the visible region, the $C_3N_4/TiO_2/Ag$−3 exhibits obviously higher absorption intensity than pure C_3N_4 and C_3N_4/TiO_2, which can be assigned to the SPR effect of Ag nanocrystals.[17,30] Moreover, the absorption edge of $C_3N_4/TiO_2/Ag$−3 has an apparent red−shift in comparison with those of pure C_3N_4 and C_3N_4/TiO_2. The band gap energy (E_g) of the sample can be estimated approximatively from a plot of $[F(R_\infty)hv]^{1/2}$ versus hv (Fig. 5b), where R, h and v are the reflectance coefficient, Planck's constant and the light frequency, respectively. The band gaps of pure C_3N_4, TiO_2, C_3N_4/TiO_2 and $C_3N_4/TiO_2/Ag$−3 are evaluated to be 2.70, 3.16, 2.66 and 2.54 eV, respectively. The result indicates that the incorporation of Ag nanocrystals can not only enhance the visible−light absorption of C_3N_4/TiO_2 but also narrow its band gap.

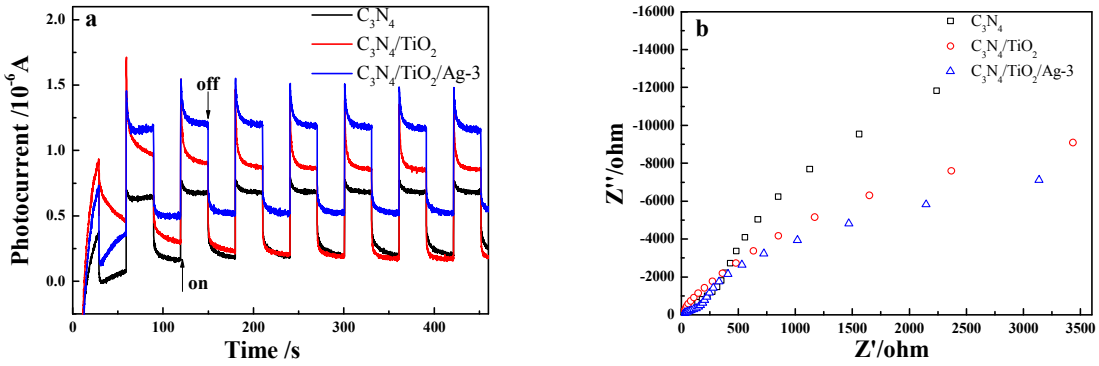

Fig. 6 (a) Transient photocurrent response and (b) EIS Nyquist plot of pure g−C_3N_4, C_3N_4/TiO_2 and C_3N_4/TiO_2/Ag−3 under simulated−sunlight irradiation.

Photocurrent responses of pure C_3N_4, C_3N_4/TiO_2 and C_3N_4/TiO_2/Ag−3 electrodes were measured to assess their photo-generated electron efficiency. As shown in Fig. 6a, a fast and uniform photocurrent response is clearly observed for each switch−on and −off event on three electrodes under simulated−sunlight irradiation. Compared with pure C_3N_4, the C_3N_4/TiO_2 exhibits a higher photocurrent response. This is caused by the conduction band match of TiO_2 with C_3N_4, which accelerates the efficient electron−hole separation of C_3N_4. After the introduction of Ag nanocrystals, the photocurrent response of C_3N_4/TiO_2/Ag elevates again, which is about 1.8 and 2.5 times higher than those of C_3N_4/TiO_2 and C_3N_4, respectively. A relatively high dark current is also observed in C_3N_4/TiO_2/Ag-3 due to the conductivity of Ag, which is also reported in other literature.[17] Additionally, EIS measurement was carried out and the EIS data were simulated using an equivalent model to investigate the charge transfer resistance of photo−generated carriers on these three film electrodes under simulated−sunlight irradiation. As can be seen from Fig. 6b, the arc radii of three samples are in the order of C_3N_4/TiO_2/Ag−3< C_3N_4/TiO_2 <C_3N_4. It is known that the arc radius of EIS Nyquist plot reflects the reaction rate occurring at the electrode surface. Usually, the sample has a low charge transfer resistance, when the arc radius of its EIS Nyquist plot is small. Therefore, the charge transfer resistance of C_3N_4/TiO_2/Ag electrode is lower than those of C_3N_4/TiO_2 and C_3N_4, in consistence with the photocurrent performance.

Photocatalytic performance

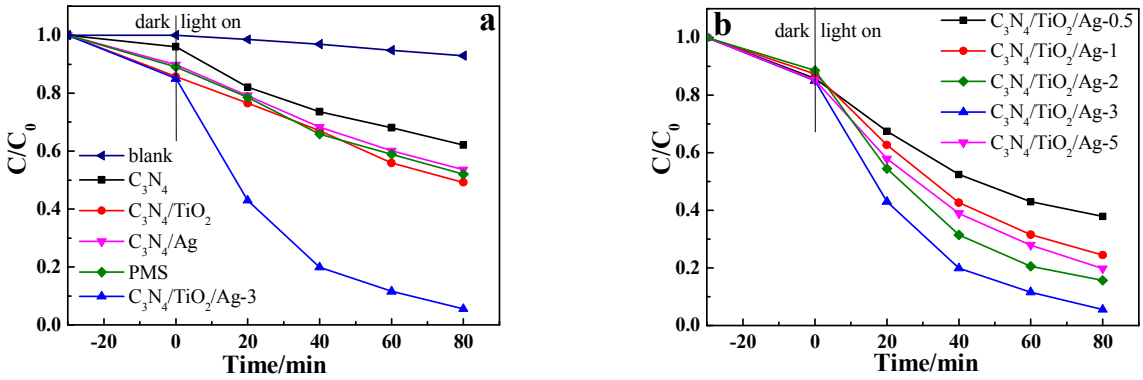

Fig. 7 Photocatalytic degradation curves of RhB over pure C_3N_4, C_3N_4/Ag, C_3N_4/TiO_2, PMS (70 wt% C_3N_4/Ag and 30 wt% TiO_2) and C_3N_4/TiO_2/Ag−3 under visible−light irradiation; (b) Effect of Ag content on the photocatalytic activity of C_3N_4/TiO_2/Ag.

The photocatalytic degradation of RhB was used to evaluate the photocatalytic activity of C_3N_4/TiO_2/Ag nanosheets under visible−light irradiation (>420 nm). The blank test confirms that RhB is only slightly degraded within 80 min in the absence of photocatalyst (Fig. 7a), indicating that the self−photolysis effect can be almost neglected. Before light irradiation, the mixed solution of RhB and photocatalyst was stirred for 0.5 h in the dark to reach the adsorption equilibrium. It is well−known that an appropriate adsorption of dye on the photocatalyst surface is beneficial to its degradation.[31] The C_3N_4/TiO_2/Ag nanosheet can decompose almost all RhB molecules within 80 min, which is remarkably higher than those of the single−, two−component and PMS samples. The kinetic study exhibits that the photocatalytic degradation of RhB over these photocatalysts belongs to the quasi−first−order kinetics. The reaction rate constant (k) of C_3N_4/TiO_2/Ag−3 is 2.18 h^{-1}, which is about 7.8 and 5.2 times higher than that of C_3N_4 and C_3N_4/TiO_2, respectively. This result can be attributed to the synergistic effect of the extended light absorption spectrum and increased light absorption intensity *via* the SPR effect of Ag NPs, the efficient electron-hole separation between matched semiconductors, and the nanosheet structure with high specific surface area (110 m^2 g^{-1}

showed in Fig. S3a). Since the reactive conditions are different, the activities of composite photocatalysts with the similar structure to $C_3N_4/TiO_2/Ag$ reported in the literatures are only compared roughly. As listed in Table 1, the $C_3N_4/TiO_2/Ag$ nanosheet prepared in this work has the better or comparative visible−light photocatalytic activity, compared with other composites.

The effect of Ag content on the photocatalytic activity of $C_3N_4/TiO_2/Ag$ nanosheets was also investigated. As illustrated in Fig. 7b, the degradation efficiency of RhB first increases and then declines with increasing the Ag content, and the $C_3N_4/TiO_2/Ag-3$ has the highest degradation efficiency in all five samples. This result is same as the changing trend of their photoluminescence spectra (Fig. S3b), which can be assigned to the balance between the SPR effect and the recombination of photo−generated carriers. When the Ag content increases, the absorbance intensity of $C_3N_4/TiO_2/Ag$ in the visible region enhances due to the SPR effect, resulting in the augment of photocatalytic activity. However, excess Ag nanocrystals are declined to act as the recombination centre of photo−generated carriers, thus lowering the photocatalytic activity. In order to investigate the versatility of this kind of materials, the photocatalytic degradation of MB was also conducted under the similar conditions (Fig. S4). It is found that the $C_3N_4/TiO_2/Ag$ nanosheet possesses the excellent photocatalytic activity for MB, and the changing trend is the same as that of RhB with the increase of Ag content. The $C_3N_4/TiO_2/Ag-3$ exhibits the highest activity in all samples, which can degrade 87% MB within 120 min. This result suggests that the $C_3N_4/TiO_2/Ag$ nanosheet has good photocatalytic ability for degrading dyes with different molecular structures and properties.

Table 1. Comparison with other photocatalytic systems

Catalyst	Degradation efficiency	Light source	$C_{catalyst}$ (mg mL^{-1})	C_{dye} (mg L^{-1})	Ref
g-C_3N_4/Ag/TiO_2 microspheres	6h, 100%	300 W (λ>420 nm)	1	MO, 13.5	19
Ag@C_3N_4 core-shell	5h, 100%	500 W (λ>420 nm)	0.5	MB, 3.74	17
C_3N_4/$BiPO_4$ core-shell	6h, 85%	500 W (λ>420 nm)	0.5	MB, 3.74	10
g-C_3N_4/TiO_2 nanosheets	5h, 80%	300 W (λ>420 nm)	1	RhB, 10	15
N-ZnO/C_3N_4 core-shell nanoplates	60 min, 100%	300 W (λ>420 nm)	0.25	RhB, 5	34
Co_3O_4-porous C_3N_4	30 min, 100%	300 W (without filter)	0.5	RhB, 5	25
g-C_3N_4/nanocage ZnS	90 min, 90%	500 W (λ>400 nm)	0.43	RhB, 5	12
g-C_3N_4/ZnO	5 h, 72%	11 W (UV light)	0.5	MB, 10	9
g- C_3N_4/rGO	75 min, 100%	1000 W (λ>400 nm)	1.6	RhB, 5	13
Au/g-C_3N_4	2.5 h, 93%	500 W (λ>400 nm)	3.0	MO, 10	14
$C_3N_4/TiO_2/Ag$ nanosheet	80 min, 100%	500 W (λ>420 nm)	0.6	RhB, 10	this work

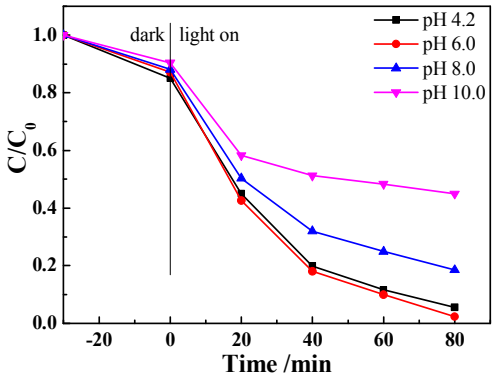

Fig. 8 Effect of pH value on the photocatalytic degradation efficiency of C_3N_4/TiO_2/Ag-3.

In order to optimize the photocatalytic condition, the effect of pH value of RhB solution on the photocatalytic activity of C_3N_4/TiO_2/Ag was investigated using C_3N_4/TiO_2/Ag−3 as a model. Fig. 8 presents the photocatalytic degradation plots of RhB solution with different pH values (4.2 (without adjustment), 6.0, 8.0, and 10.0). With increasing the pH value, the degradation rate of RhB first increases and then decreases, and the C_3N_4/TiO_2/Ag−3 demonstrates the highest activity at pH 6.0. The influence of pH on the dye degradation process is mainly attributed to the surface charge variation of photocatalyst and dye molecules.[31] It is known that the point of zero charge (pH_{pzc}) of TiO_2 is at about pH 5.5 and RhB is a cationic dye molecule. The pH change can influence the electric properties of TiO_2 surface and RhB, and then affect the adsorption of RhB molecules onto the TiO_2 surface,[32] an important step for the photocatalytic oxidation to take place. When pH<5.5, the TiO_2 surface brings the positive charge and repulses RhB molecules with same charge, thus inhibiting the adsorption of RhB onto the TiO_2 surface. Therefore, the C_3N_4/TiO_2/Ag nanosheet exhibits a low photocatalytic activity at low pH value. When pH>5.5, the TiO_2 surface brings the negative charge and attracts RhB molecules with opposite charge, thereby accelerating the adsorption of RhB onto the TiO_2 surface. Therefore, the C_3N_4/TiO_2/Ag nanosheet exhibits a higher photocatalytic activity at high pH value in comparison with that at low pH value. However, the negative charge on the TiO_2 surface can repulse OH^- at the same time, thus supressing the •OH production. As a result, the photocatalytic activity of C_3N_4/TiO_2/Ag decreases gradually with the increase of pH value at pH > 6.[32,33]

Photocatalytic mechanism

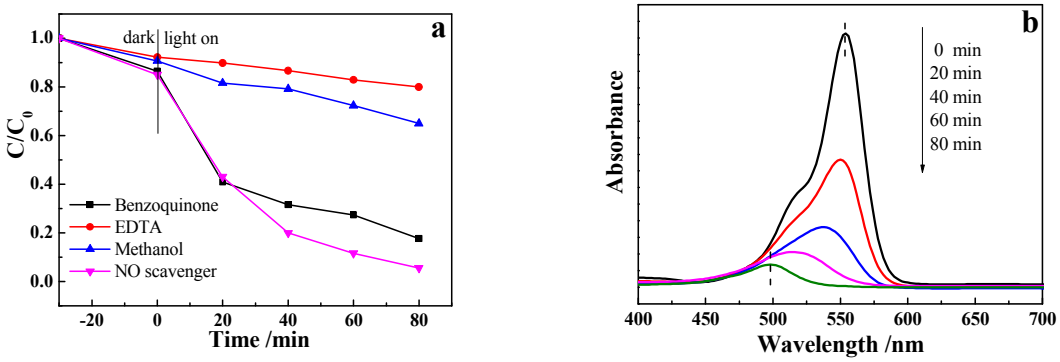

Fig. 9 (a) Effect of different scavengers on the photocataltic degradation of RhB over C_3N_4/TiO_2/Ag-3; (b) UV-vis spectrum changes of RhB over C_3N_4/TiO_2/Ag-3 during the photocatalytic process.

To uncover the photocatalytic mechanism of C_3N_4/TiO_2/Ag, a radical trapping experiment was performed to explore the reactive radical species involved in the photocatalytic process. It is well−known that three reactive radicals containing h^+, •OH, and $•O^{2-}$, are produced during the photocatalytic process, which act as the important roles in the degradation of organic pollutants.[34] Thereby, three chemicals including benzoquinone, EDTA and methanol were employed as the scavenger of $•O^{2-}$, hole and •OH, respectively. As presented in Fig. 9a, the photocatalytic activity of C_3N_4/TiO_2/Ag is considerably suppressed by EDTA and methanol, while slightly inhibited by benzoquinone. This result indicates that the h^+ and ·OH are the main reactive species involved in the RhB degradation over C_3N_4/TiO_2/Ag, while the $•O^{2-}$ is produced only a few during the photocatalytic process. It was further proved by the UV−vis spectrum change of RhB during the photocatalytic degradation process over C_3N_4/TiO_2/Ag−3. From Fig. 9b, it can be seen that the absorption peak gradually shifts from 553 to 498 nm with the prolongation of reaction time. This result indicates that the *N*-de-ethylation process is the main degradation process of RhB. In detail, this process can produce the intermediates with different numbers of N−ethyl groups, which are removed sequentially from the

parent RhB molecules, leading to the absorption peak of RhB blue shift; further confirming that the •OH is the major reactive radical species.[35,36]

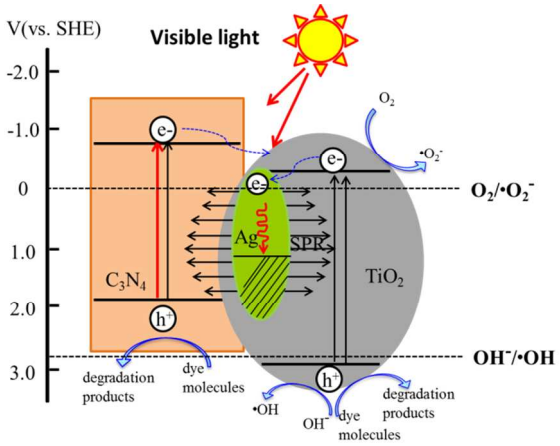

Scheme 2 Schematic diagram for the photocatalytic mechanism of $C_3N_4/TiO_2/Ag$ under visible−light irradiation.

On the basis of above results, a tentative photocatalytic degradation mechanism of RhB over the $C_3N_4/TiO_2/Ag$ nanosheet is proposed in Scheme 2. Under visible−light irradiation, the C_3N_4 nanosheet absorbs the visible light and then is excited. The generated electrons can react with O_2 adsorbed on the C_3N_4 nanosheet to produce $•O_2^-$, thus oxidizing RhB further or transferring into the CB of TiO_2. The generated holes can only degrade the RhB molecules directly, because the VB potential of C_3N_4 (+1.57 eV vs. NHE) is more negative than the standard redox potential of $E(·OH/OH^-)$ = +1.99 eV (vs. NHE), causing that the holes in the VB of C_3N_4 cannot oxidize OH^- to generate ·OH. At the same time, Ag nanocrystals generate intense electric fields on their surface at the plasmon frequency under visible−light irradiation,[16] which induces the electron transition of adjacent TiO_2 from VB to CB, keeping the holes in the VB of TiO_2.[16] The holes in the CB of TiO_2 have more positive potential to oxidize OH^- and generate active ·OH radicals with powerful oxidization capability, thereby degrading the RhB molecules adsorbed on the TiO_2 surface. Meanwhile, these holes can also transfer into the VB of C_3N_4 nanosheet and further degrade the RhB molecules. The photo−generated electrons react with O_2 adsorbed on the TiO_2 surface to produce $•O_2^-$, together with the electrons transferred from the CB of C_3N_4 nanosheet. In addition, the presence of the heterojunction between Ag and TiO_2 facilitates the electron transfer and then inhibits the recombination of photo–generated carriers. During the photocatalytic process, Ag nanocrystals may lose electron and turn to Ag^+ due to the SPR effect, which releases to the reactive solution subsequently.[20] However, the degradation efficiency of RhB over $C_3N_4/TiO_2/Ag$ only reduces from 94.5% to 90.3% after 4 recycles (Fig. S5), indicating that the $C_3N_4/TiO_2/Ag$ nanosheet is chemically stable and mechanically robust during the photocatalytic process. Therefore, the conversion of Ag to Ag^+ does not almost influence the stability of $C_3N_4/TiO_2/Ag$ nanosheets.

Conclusion

In this study, the $C_3N_4/TiO_2/Ag$ nanosheet with excellent photoelectric and photocatalytic performances has been synthesized *via* a biomimetic strategy under mild conditions. In the prepared $C_3N_4/TiO_2/Ag$ nanosheet, TiO_2 nanoparticles about 10 nm in size are dispersed uniformly on the C_3N_4 nanosheet, and Ag nanocrystals about 5 nm in diameter grow around the TiO_2 and form the heterojunction structure with TiO_2. During the biomimetic synthetic process, the diHPP molecules act as both an anchor and a reducer for the *in situ* nucleation and growth of Ag nanocrystals on the C_3N_4/TiO_2 surface. The $C_3N_4/TiO_2/Ag$ nanosheet demonstrates much higher photocatalytic activity than its single− and two−component counterparts under visible light, which is attributed to the band match of C_3N_4 with TiO_2 and the SPR effect and inhibiting effect for photo−generated carriers of Ag nanocrystals. Hopefully, this study may offer some inspiration for the design and green synthesis of semiconductor-based nanocomposites with enhanced visible−light photocatalytic activity.

Acknowledgements

This work is supported by National Science Fund for Distinguished Young Scholars (21125627) and the Program of Introducing Talents of Discipline to Universities (No. B06006).

Notes and references

[a] *Key Laboratory for Green Technology, School of Chemical Engineering and Technology, Tianjin University, Tianjin 300072, China. Fax: 86-22-27406646. Tel: 86-22-27406646. E-mail: zhyjiang@tju.edu.cn.*
[b] *Key Laboratory of Systems Bioengineering of Ministry of Education, School of Chemical Engineering and Technology, Tianjin University, Tianjin 30072, China*
[c] *School of Environmental Science and Engineering, Tianjin University, 300072 Tianjin, China*
[d] *Collaborative Innovation Center of Chemical Science and Engineering (Tianjin), Tianjin 300072, China*

Electronic Supplementary Information (ESI) available: [details of any supplementary information available should be included here]. See DOI: 10.1039/b000000x/

1 H. Dotan, O. Kfir, E. Sharlin, O. Blank, M. Gross, I. Dumchin, G. Ankonina and A. Rothschild, *Nat. Mater.* 2013, **12**, 158–164.
2 J. Liu, Y. Yang, N. Y. Liu, Y. Z. Han, X. Zhang, H. Huang, Y, Lifshitz, S. T. Lee, J. Zhong and Z. H. Kang, *Science* 2015, **347**, 970–974.
3 C. C. Chen, W. H. Ma and J. C. Zhao, *Chem. Soc. Rev.* 2010, **39**, 4206–4219.
4 X.C. Wang, K. Maeda, A. Thomas, K. Takanabe, G. Xin, J. M. Carlsson, K. Domen and M. Antonietti, *Nat. Mater.* 2008, **8**, 76–80.
5 X. C. Wang, S. F. Blechert and M. Antonietti, *ACS Catal.* 2012, **2**, 1596–1606.
6 H. L. Wang, L. S. Zhang, Z. G. Chen, J. Q. Hu, S. J. Li, Z. H. Wang, J. S. Liu and X. C. Wang, *Chem. Soc. Rev.* 2014, **43**, 5234–5244.
7 H. Tong, S. H. Ouyang, Y. P. Bi, N. Umezawa, M. Oshikiri and J. H. Ye, *Adv. Mater.* 2012, **24**, 229–251.
8 J. J. Zhu, P. Xiao, H. L. Li and S. A. Carabineiro, *ACS Appl. Mater. Interfaces* 2014, **6**, 16449–16465.
9 Y. J. Wang, R. Shi, J. Lin and Y. F. Zhu, *Energ. Environ. Sci.* 2011, **4**, 2922–2929.
10 C. S. Pan, J. Xu, Y. J. Wang, D. Li and Y. F. Zhu, *Adv. Funct. Mater.* 2012, **22**, 1518–1524.
11 J. Fu, B. B. Chang, Y. L. Tian, F. N. Xi and X. P. Dong, *J. Mater. Chem. A* 2013, **1**, 3083–3090.
12 J. Wang, P. Guo, Q. S. Guo, P.G. Jönsson and Z. Zhao, *CrystEngComm* 2014, **16**, 4485–4492.
13 Y. B. Li, H. M. Zhang, P. R. Liu, D. Wang, Y. Li and H. J. Zhao, *Small* 2013, **9**, 3336–3344.
14 N. Y. Cheng, J. Q. Tian, Q. Liu, C. J. Ge, A. H. Qusti, A. M. Asiri, A. O. Al-Youbi and X. P.Sun, *ACS Appl. Mater. Interfaces* 2013, **5**, 6815–6819.
15 Z. W. Tong, D. Yang, T. X. Xiao, Y. Tian and Z. Y. Jiang, *Chem. Eng. J.* 2015, **260**, 117–125.
16 K. C. Awazu, M. Fujimaki, C. Rockstuhl, J. J. Tominaga, H. Murakami, Y. Ohki, N. Y. Yoshida and T. Watanabe, *J. Am. Chem. Soc.* 2008, **130**, 1676–1680.
17 X. J. Bai, R. L. Zong, C. X. Li, D. Liu, Y. F. Liu and Y. F. Zhu, *Appl. Catal. B* 2014, **147**, 82-91.
18 M. K. Kumar, S. Krishnamoorthy, L. K. Tan, S. Y. Chiam, S. Tripathy and H. Gao, *ACS Catal.* 2011, **1**, 300–308.
19 Y. F. Chen, W. X. Huang, D. L. He, Y. Situ and H. Huang, *ACS Appl. Mater. Interfaces* 2014, **6**, 14405–14414.
20 D. Yang, Y. Y. Sun, Z. W. Tong, Y. Tian, Y. B. Li and Z. Y. Jiang, *J. Phys.Chem. C* 2015, **119**, 5827–5835.
21 K. C. L. Black, Z. Liu and P. B. Messersmith, *Chem. Mater.* 2011, **23**, 1130–1135.
22 P. Niu, L. Zhang, G. Liu and H. M. Cheng, *Adv. Funct. Mater.* 2012, **22**, 4763–4770.
23 S. Bahri, C. M. Jonsson, C. L. Jonsson, D. Azzolini, D. A. Sverjensky and R. M. Hazen, *Environ. Sci. Technol.* 2011, **45**, 3959–3566.
24 W. J. Ong, L. L. Tan, S. P. Chai and S. T. Yong, *Chem. Commun.* 2015, **51**, 858–861.
25 J. D. Hong, S. M. Yin, Y. X. Pan, J. Y. Han, T. H. Zhou and R. Xu, *Nanoscale* 2014, **6**, 14984–14990.
26 Y. Q. Shi, S. H. Jiang, K. Q. Zhou, C. L. Bao, B. Yu, X. D. Qian, B. B. Wang, N. N. Hong, P. Y. Wen, Z. Gui, Y. Hu and R. K. K. Yuen, *ACS Appl. Mater. Interfaces* 2013, **6**, 429–437.
27 X. C. Wang, J. C. Yu, H. Y. Yip, L. Wu, P. K. Wong and S. Y. Lai, *Chem. Eur. J.* 2005, **11**, 2997–3004.
28 X. J. Wang, W. Y. Yang, F. T. Li, Y. B. Xue, R. H. Liu and Y. J. Hao, *Ind. Eng. Chem. Res.* 2013, **52**, 17140–17150.
29 C. Liu, D. Yang, Y. Jiao, Y. Tian, Y. G. Wang and Z. Y. Jiang, *ACS Appl. Mater. Interfaces* 2013, **5**, 3824–3832.
30 Y. Y. Wen, H. M. Ding and Y. K. Shan, *Nanoscale* 2011, **3**, 4411–4417.
31 A. N. Ejhieh and M. K. Shamsabadi, *Chem. Eng. J.* 2013, **228**, 631–641.
32 U.G. Akpan and B.H. Hameed, *J. Hazard. Mater.* 2009, **170**, 520–529.
33 M. Pelaez, N. T. Nolan, S. C. Pillai, M. K. Seery, P. Falaras, A. G. Kontos, P. S. M. Dunlop, J. W. J. Hamilton, J. A. Byrne, K. O'Shea, M. H. Entezari and D. D. Dionysiou, *Appl. Catal. B.* 2012, **125**, 331–349.
34 S. Kumar, A. Baruah, S. Tonda, B. Kumar, V. Shanker and B. Sreedhar, *Nanoscale* 2014, **6**, 4830–4842.
35 P. X. Lei, C. C. Chen, J. Yang, W. H. Ma, J. C. Zhao and L. Zang, *Environ. Sci. Technol.* 2005, **39**, 8466–8474.
36 H. B. Fu, S. C. Zhang, T. G. Xu, Y. F. Zhu and J. M. Chen, *Environ. Sci. Technol.* 2008, **42**, 2085–2091.